

Characterization of Damage Evolution in SiC Particle Reinforced Al Alloy Matrix Composites by *In-Situ* X-Ray Synchrotron Tomography

J.J. WILLIAMS, N.C. CHAPMAN, V. JAKKALI, V.A. TANNA, N. CHAWLA, X. XIAO, and F. De CARLO

We carried out a detailed investigation of the damage behavior of SiC particle reinforced 2080 Al alloy matrix composites by *in-situ* X-ray synchrotron tomography. We studied the tensile damage behavior of a peak-aged aluminum matrix composite. The main damage mode was SiC particle fracture with a very small contribution from void growth. The onset of damage takes place very close to the ultimate tensile strength of the composite. Particle fracture damage is stochastic in nature and is confined to a small distance from the fracture plane. Minimal void growth is observed, primarily at pre-existing microscopic voids from processing. Microstructure-based simulations, based on two-dimensional (2-D) images from the tomography data sets, show the importance of particle distribution and morphology on the evolution of plastic strain and damage in the composite.

DOI: 10.1007/s11661-011-0718-8

© The Minerals, Metals & Materials Society and ASM International 2011

I. INTRODUCTION

THE field of materials science and engineering is based on the fundamental principle that microstructure controls properties. Traditionally, the study of material structure was limited by two-dimensional (2-D) analyses. This approach is often inaccurate or inadequate for solving many cutting-edge problems. In addition, it is often laborious and time-consuming. We can now use three-dimensional (3-D) tools and analyses to resolve time-dependent four-dimensional (4-D) evolution of a variety of important phenomena.^[1] These include an understanding of time-dependent deformation structures, compositional information, magnetic domains, interfacial reactions, *etc.* Furthermore, advances in 3-D and 4-D computational tools and methods enabled the analysis of large experimental data sets, as well as simulation and prediction of material behavior. Figure 1 shows a variety of techniques, as a function of length scale, used to characterize materials in three dimensions.

The design and development of high-performance composites requires a thorough understanding of microstructure and its effect on properties. Metal matrix composites (MMCs) have a combination of high strength, high stiffness, and low density.^[2] The damage behavior of MMCs was studied extensively by a

combination of traditional mechanical testing, microstructural characterization, and postexperiment fractographic analysis. It is generally agreed that damage in extruded ceramic particle reinforced MMCs takes place by a combination of particle fracture and matrix void growth. An understanding of the precise nature of these damage mechanisms was limited by examinations of the 2-D fracture surface or polished cross section of the material. In both cases, the approach is laborious and limited by the 2-D nature of the analysis. Sampling a representative volume of the microstructure by such analyses is also difficult.

With the recent development of new 3-D characterization tools, a clear, accurate, and quantitative picture of the deformation behavior of MMCs can be obtained. Several techniques were used for visualization of microstructures in three dimensions. Serial sectioning techniques using mechanical polishing coupled with optical microscopy^[3,4] or focused ion beam milling^[5-7] and image reconstruction were used. While serial sectioning is a powerful technique for generating virtual 3-D microstructures, it is time consuming and destructive.

X-ray tomography is an excellent technique that eliminates destructive cross sectioning and allows for superior resolution and image quality with minimal sample preparation.^[8,9] 3-D visualization and quantification of heterogeneous microstructures by X-ray tomography was successfully performed in Sn-rich alloys,^[10] powder metallurgy steels,^[11] metal matrix composites,^[12-16] and aluminum and copper alloys.^[17,18] In addition to visualization, such microstructural data sets can be incorporated into finite element models to predict the onset of local damage mechanisms and macroscopic deformation behavior.^[15,19-21]

A sound understanding of damage in MMCs requires adequate visualization and quantification of fracture

J.J. WILLIAMS, Research Scientist, N.C. CHAPMAN and V.A. TANNA, Undergraduate Research Assistants, V. JAKKALI, Graduate Research Assistant, and N. CHAWLA, Professor, are with the Materials Science and Engineering Department, Arizona State University, Tempe, AZ 85287-6106. Contact e-mail: nchawla@asu.edu X. XIAO, Assistant Physicist, and F. De CARLO, Group Leader, are with the X-ray Imaging Group, X-ray Science Division, Advanced Photon Source, Argonne National Laboratory, Argonne, IL 60439.

Manuscript submitted November 2, 2010.

Article published online May 4, 2011

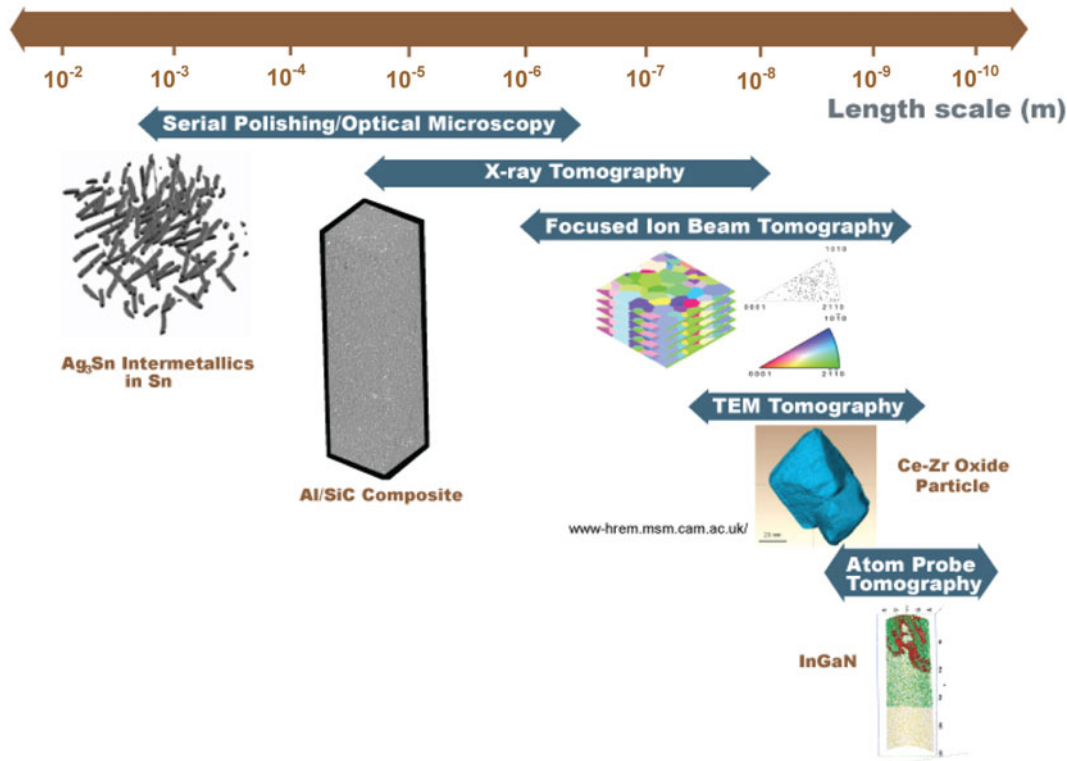


Fig. 1—Techniques used for 3-D and 4-D materials science vs length scale.

based on the 3-D microstructure. More importantly, it requires a significant amount of statistical characterization and analysis, particularly of particle fracture and void growth. The distribution of defects and voids, before and after deformation, needs to be quantified. While several studies on damage of metallic materials were conducted by X-ray synchrotron tomography, relatively few reported on *in-situ* methods. *In-situ* techniques are particularly suited for studying the initiation and evolution of damage in metal matrix composites. A clear understanding of the sequence of particle fracture and void growth and the relative importance of each type of mechanism can be obtained from *in-situ* studies.

In this work, we have carried out a detailed investigation of the damage behavior of SiC particle reinforced 2080 Al alloy matrix composites by *in-situ* X-ray synchrotron tomography. The evolution of damage in tension was quantified. The role of particle fracture and void growth in incubation and evolution of damage was studied. Based on this, a detailed understanding of the micromechanisms of fracture was obtained. Finally, 2-D images were used to conduct microstructure-based finite element modeling using the actual microstructure as a basis.

II. MATERIALS AND EXPERIMENTAL PROCEDURE

The material used in this study was a 2080 aluminum alloy (3.6 pct Cu, 1.9 pct Mg, 0.25 pct Zr) reinforced

with 20 vol pct SiC particles (average particle size of 25 μm). The materials were processed by blending SiC and Al powders, compacting the powder mixture, hot pressing, and hot extrusion (Alcoa Inc., Alcoa, PA). Details of the powder metallurgy process for fabrication of these composite materials can be found elsewhere.^[22]

The X-ray synchrotron tomography was performed on as-processed and tensile fractured composites at the Advanced Photon Source (APS) at Argonne National Laboratory. The fast microtomography system developed at the beamline 2-BM of the APS offers near video-rate acquisition of tomographic data at micrometer spatial resolution. Every sample is fully analyzed within 2 to 3 minutes, providing immediate feedback on the quality of the results. The tomography system of the APS beamline 2-BM was described in detail elsewhere.^[23–25] The double multilayer monochromator installed at beamline 2-BM covers energies between 5 and 30 keV. Using the standard detector, a 2048 \times 2048 pixel CoolSnap K4 CCD camera coupled with a LuAG:Ce scintillator screen, typical exposure times between 80 and 200 ms per projection were obtained. In this configuration, we collected a projection every 1/8 deg for 180 deg. Including the readout time and disk input/output, the tomography can be completed in about 15 minutes.

Uniaxial tensile tests were carried *in situ* in the synchrotron on dog-bone specimens with a square cross section. Samples were sectioned using electrical discharge machining (EDM). The specimen's gage section was 2.5-mm long with a 0.75-mm square cross section (Figure 2(a)). Specimens were machined parallel to the

extrusion axis. Samples were loaded by a stepped displacement; *i.e.*, the actuator was displaced until the desired load was achieved. A tomography scan was performed at each displacement. This was done at several increasing displacement until failure. The load cell had a 500 N capacity, and the stepper motor had a captive linear actuator capable of 8 μm per step and 12-mm stroke (Figure 2(b)).

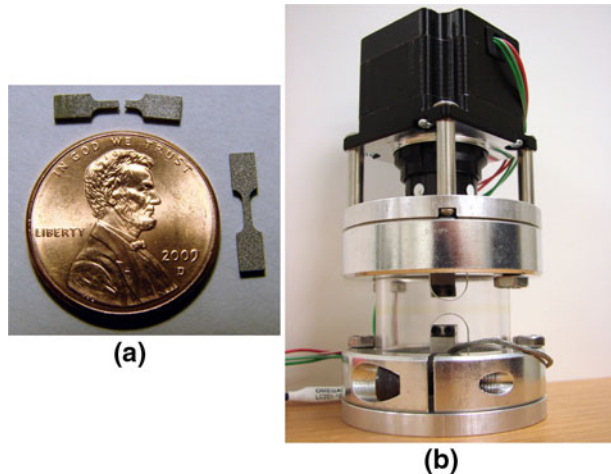


Fig. 2—(a) Tensile specimens used for *in-situ* tensile testing, machined by EDM, and (b) *in-situ* loading stage.

III. RESULTS AND DISCUSSION

The loading stage used for *in-situ* tomography has a Poly(methyl methacrylate) (PMMA) sleeve that connects the two sides of the stage and enables load to be applied to the specimen. In order to facilitate the loading of the miniature specimen, two holes were incorporated into the sleeve. A simple linear elastic finite element analysis (Cosmos Xpress, Solidworks 2008, Concord, MA) was conducted to determine the stresses and displacements in the sleeve (Figure 3(a)). The modulus of the PMMA was taken as 2.4 GPa and the Poisson's ratio as 0.35. The displacement of bottom face was constrained and a compressive load of 200 N was applied to the opposite face. The stress in the region between the holes was only about 0.1 MPa. The displacement in the sleeve was also quite small, on the order of a few micrometers. In addition, experiments at the maximum load applied to the MMC specimen were conducted to determine the creep rate of the sleeve during the 30-minute tomography operation (Figure 3(b)). A negligible displacement rate of 2.5 nm/min was obtained, which did not significantly affect our experiments.

Figure 4 shows the stress-strain curve for a 2080/SiC/20_p composite tested *in situ*. The data points indicate points where the experiment was paused for tomography. The composite had a strength of about 425 MPa with a strain to failure of about 1.6 pct. Figure 5 shows the evolution of damage, in two separate regions of the

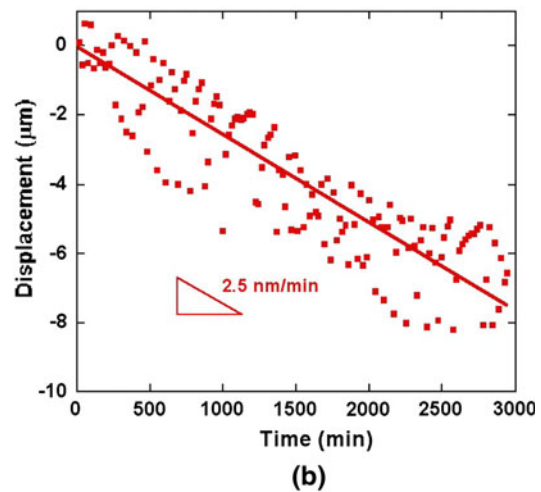
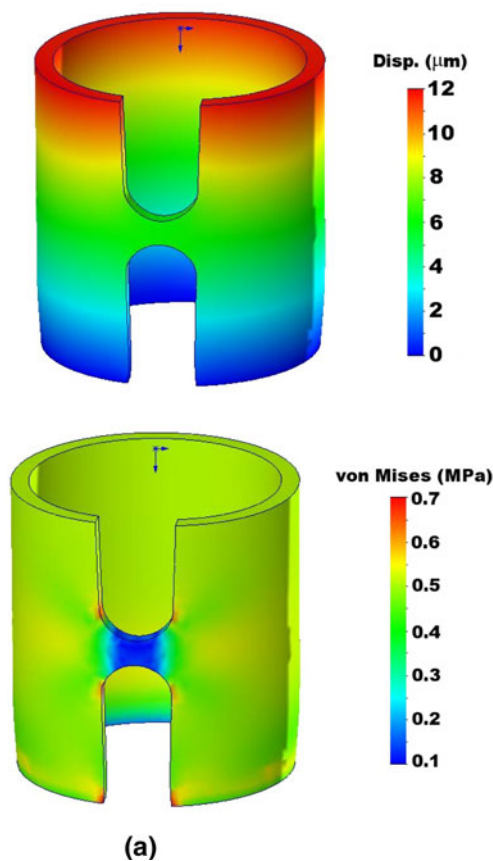


Fig. 3—(a) Finite element modeling of displacement and stress in PMMA sleeve. (b) Experimental measurements of displacement in sleeve, at maximum load, for 30 min (time required for tomography). Both computed stresses and measured displacements are negligible.

microstructure, at three different stresses. The onset of damage appears to begin very close to the ultimate strength, at about 440 MPa. This damage is primarily dominated by particle fracture, which begins around

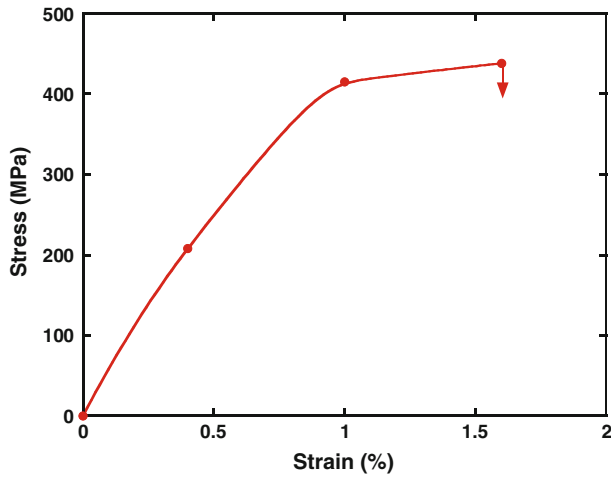


Fig. 4—Stress-strain curve of 2080/SiC/20_p composite determined *in situ* in the synchrotron. The solid points indicate where the experiment was paused for tomography. This curve is very similar to the stress-strain behavior measured on a conventional microforce testing system.

1 pct strain. Figure 5(a) shows the onset of particle fracture through the center of the particle, likely at a flaw within the particle, and propagates out to the matrix. Figure 5(b) shows that most of the particle fracture is observed very close to the fracture stress. Williams *et al.*^[16] recently showed, through analysis of particle fracture statistics obtained from X-ray synchrotron tomography, that the probability of particle fracture is controlled by particle size and aspect ratio. It is a stronger function of aspect ratio than of particle size. They showed that, using the statistics from the 3-D tomography, aspect ratio and particle size are important parameters in determining the probability of fracture in the SiC particles. Some instances of localized void growth are also observed, particularly at the sharp corners of the SiC particles, but also in regions where particles are very closely spaced. Here, the thin layer of matrix is highly constrained and under a triaxial state of stress, which promotes void growth. The degree of void growth was quite limited, however, and seemed to take place primarily at pre-existing voids from processing.

The degree of particle fracture, as a function of applied stress, was quantified throughout the gage length. This is shown in Figure 6. The composite had some particles fracture prior to testing. These particles fractured during the extrusion process. Local increases in particle fracture density are observed, with increasing stress. A slight

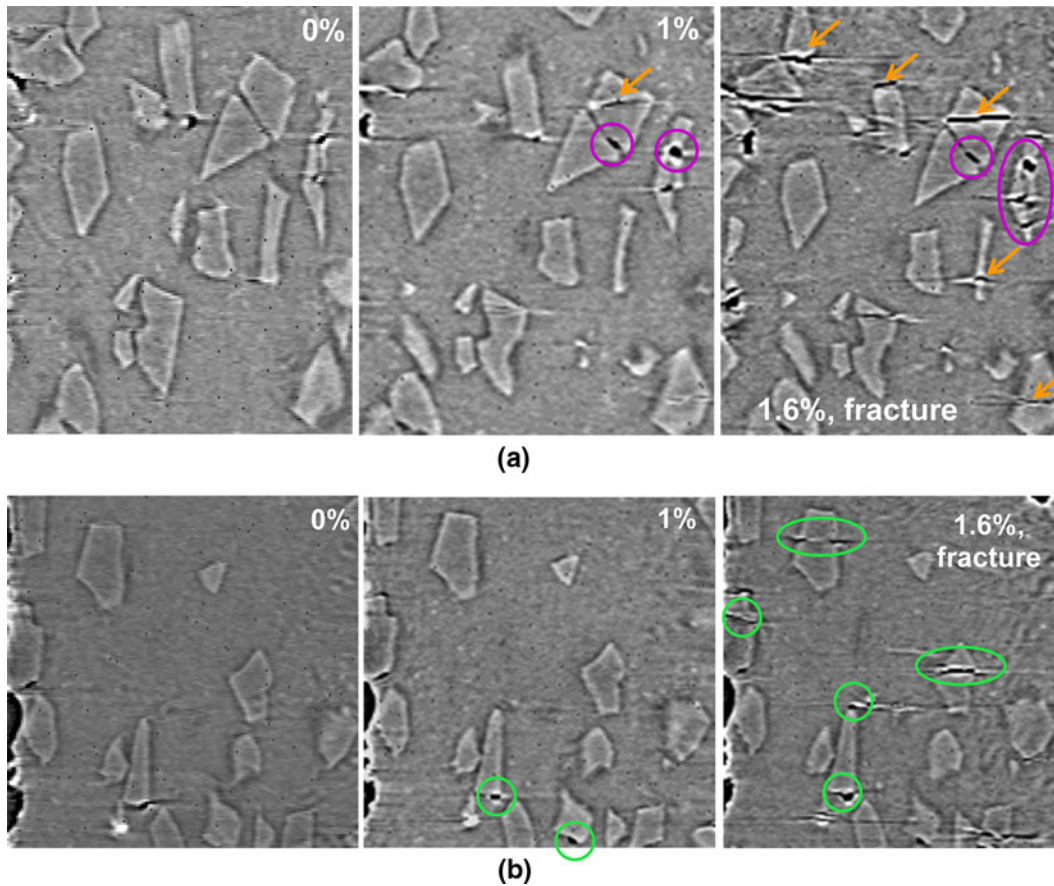


Fig. 5—Evolution of damage as a function of applied stress by *in-situ* X-ray tomography. At 0 to 0.4 pct strain, no damage is observed. At 1 pct, void growth begins at sharp corners and regions of high constraint and triaxiality. At fracture (1.6 pct), particle fracture is quite predominant. (a) Region 1 and (b) region 2.

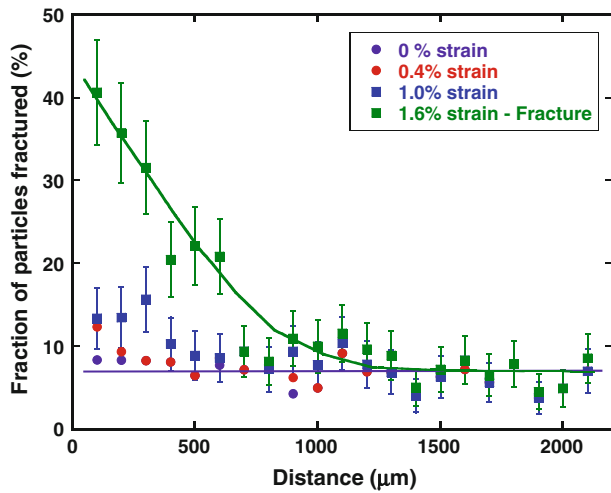


Fig. 6—Evolution of damage in the form of particle fracture over the gage length by *in-situ* X-ray tomography. Localized increases in particle fracture are observed, but most of the damage takes place between 440 MPa and fracture at 495 MPa.

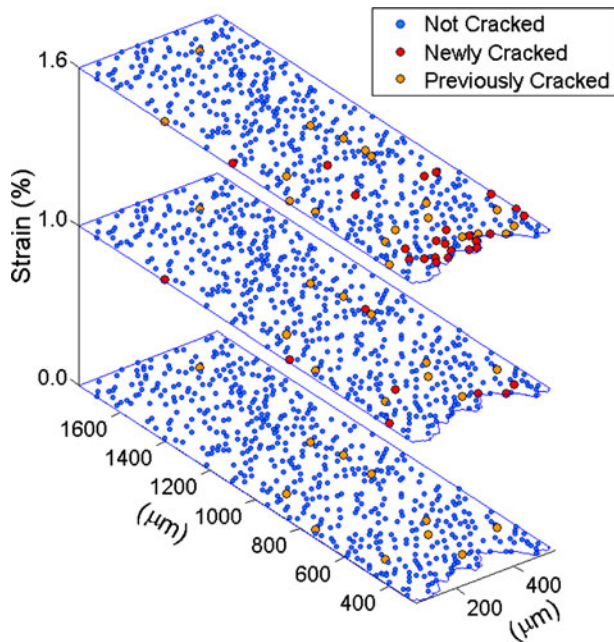


Fig. 7—Graphical representation of the relative position of SiC particles in the same slice as a function of strain (z -axis). Blue points represent particles that are not cracked. Red points and orange points are particles that are “newly” cracked and “previously cracked,” respectively, relative to the previous strain level.

increase in particle fracture is observed, at 1 pct strain, close to the eventual fracture plane and foreshadowing where fracture would take final place. The largest increase in particle fracture, as shown in Figure 5, is between 1 pct and the fracture strain of 1.6 pct, at the fracture plane. The density of fracture particles is highest at this plane and decreases sharply over a distance of about 1 mm, as shown by Williams *et al.*^[16] Figure 7 graphically shows the evolution of fracture in the SiC particles, in a 2-D slice, as a function of strain. The blue

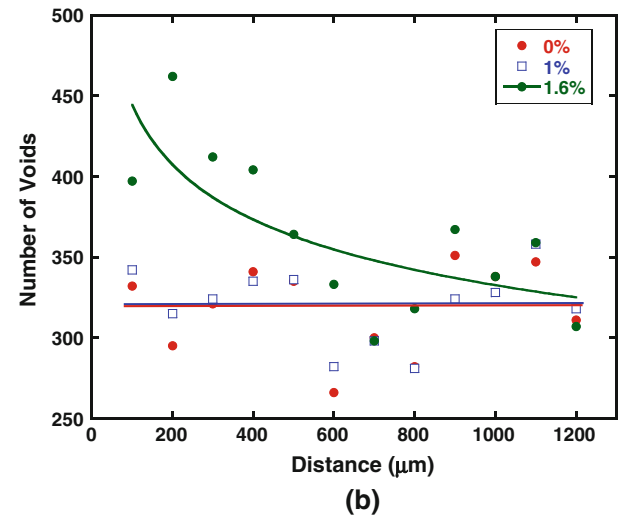
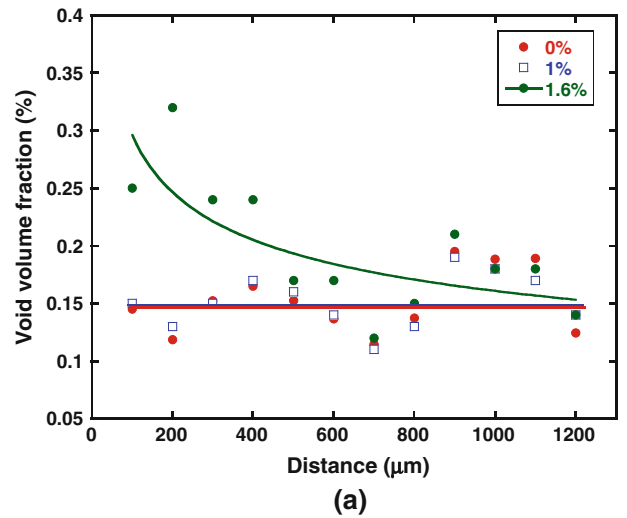


Fig. 8—Quantification of voids as a function of applied strain: (a) void volume fraction and (b) number of voids. Note that the onset of damage appears to be very close to the fracture strain of 1.6 pct, as in the case of particle fracture.

particles are undamaged. Prior to straining, some particles that cracked during the extrusion process are shown (in orange). At 1 pct strain, the stochastic process of particle fracture begins with isolated particle fracture taking place. The onset of fracture begins at a large fraction of the fracture strain, *i.e.*, quite late in the tensile test. At fracture, at a strain of 1.6 pct, a large density of red points, indicating fractured SiC particles, is shown very close to the fracture plane.

Void growth was also quantified as a function of applied strain. The voids were differentiated from cracks by morphological distinction obtained by image analysis. This process is described elsewhere.^[16] Figure 8 shows the number of voids and void volume fraction, as a function of strain along the gage length of the specimen. The degree of void growth is not very large. An average equivalent spherical diameter of about $7 \mu\text{m}$ was measured prior to loading, while at fracture, it increased only slightly to $8 \mu\text{m}$, or about 14 pct. Similar

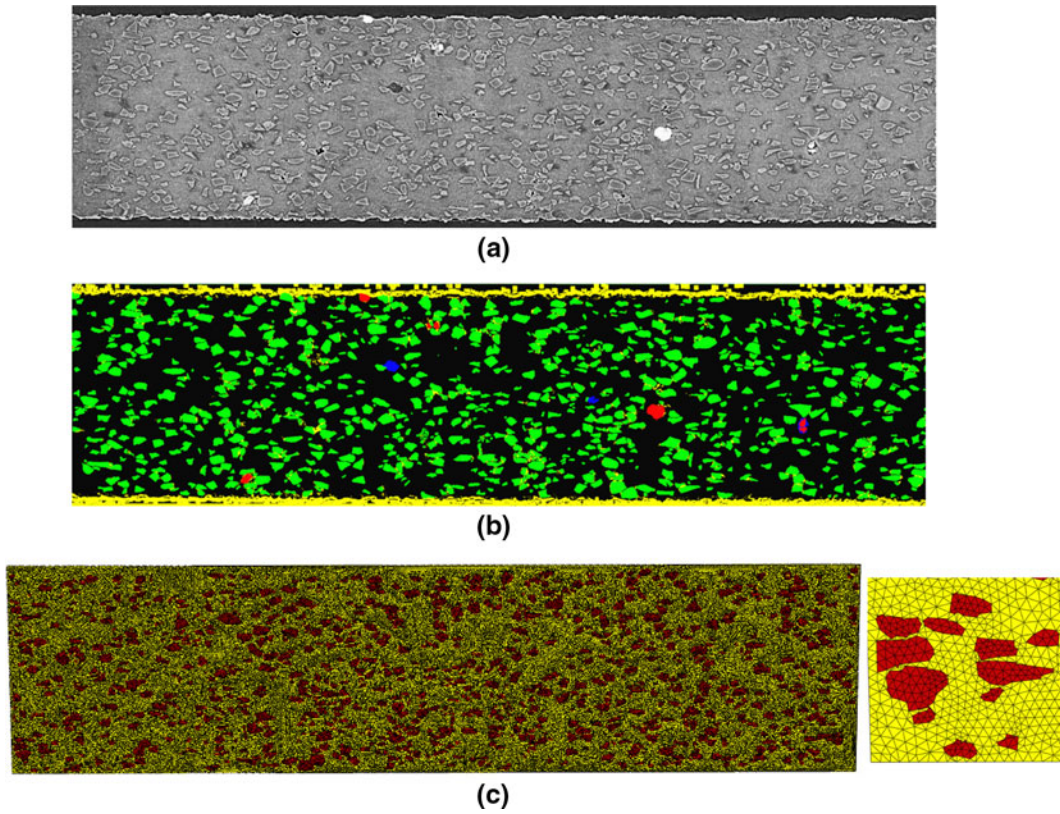


Fig. 9—Schematic of microstructure-based simulations from X-ray synchrotron tomography: (a) 2-D slice from X-ray synchrotron data, (b) segmented image, and (c) finite element mesh.

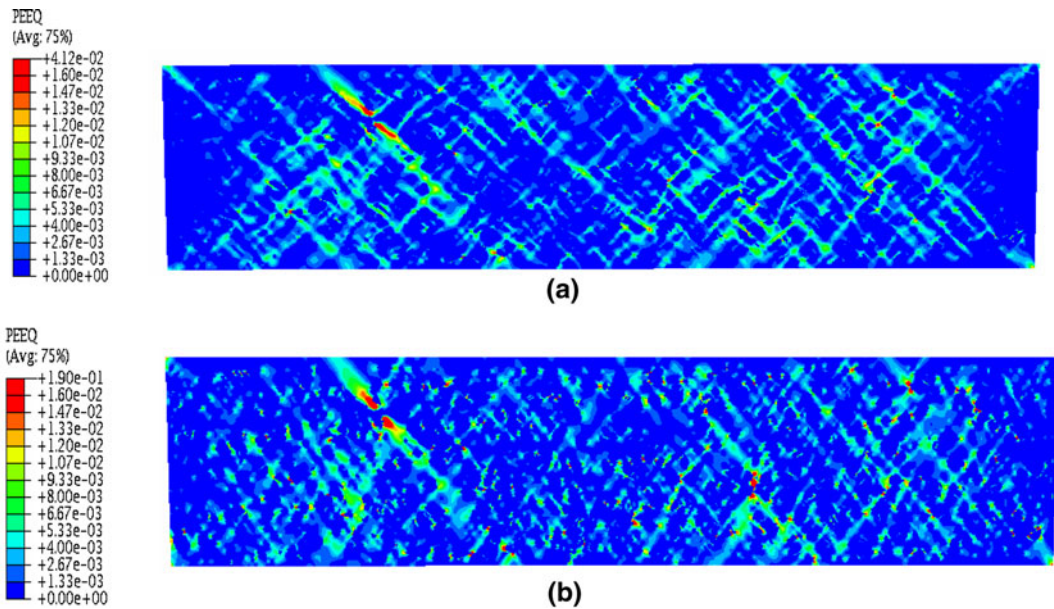


Fig. 10—Finite element simulations based on actual microstructures: (a) plane strain and (b) plane stress. Shear bands between SiC particles are observed. Larger plastic strains are observed under plane stress.

to the evolution of particle fracture, the onset of void growth almost coincides with the fracture strain. This is consistent with other experimental findings, where, in

peak-aged alloys, damage is controlled by particle fracture, rather than void growth.^[2] This is because the matrix strength is quite high as is the particle/matrix

interface strength. Thus, the particles fractured prior to matrix void growth or interfacial debonding.

In addition to quantifying the evolution of damage as a function of time, microstructure-based modeling can also be conducted using X-ray tomography data sets. The methodology for exporting the image into a finite element modeling program is provided elsewhere.^[26,27] A 2-D image of the microstructure of the 2080/SiC_p composite was imported into a dedicated meshing program (Hypermesh, Troy, MI) to generate the mesh. The SiC particles were meshed initially to generate a fine mesh on the particles. The Al matrix was meshed to maintain nodal connectivity with the nodes on the SiC particles. The model was meshed using linear triangular elements (three nodes). The total model had about 115,000 elements.

Figure 9 shows the segmented image and the meshed image prior to modeling. Finite element modeling was conducted using Abaqus (Simulia, Providence, RI). The particle was modeled as linear elastic, with a modulus of 410 GPa and Poisson's ratio of 0.19. The aluminum alloy matrix was modeled as an elastic-plastic material, with a modulus of 74 GPa and Poisson's ratio of 0.33. The plastic portion of the constitutive law was obtained by experiments on the unreinforced matrix. The boundary conditions are as follows. The left side of the image was constrained in the x direction. The displacement was applied to the right edge of the image to a strain of 0.5 pct. The constitutive behavior of the particles and the matrix was as follows. Figure 10 shows the equivalent plastic strain in the model in (a) plane stress and (b) plane strain. The plane stress model exhibits a higher degree of plasticity. Shear bands in both models are observed, which are disturbed by the distribution of SiC particles. Particle clusters are regions for strain localization and exhibit a higher concentration of plastic strain.

IV. SUMMARY

A systematic study of the 3-D microstructure of SiC particle-reinforced 2080 Al alloy matrix composites, by *in-situ* X-ray synchrotron tomography, was conducted. The following important points can be made, as a result of this work.

1. *In-situ* tomography is an excellent means of quantifying the damage in metallic materials. In the peak-aged aluminum matrix composites studied here, the main damage mode was SiC particle fracture with a very small contribution from void growth.
2. The onset of damage takes place very close to the ultimate tensile strength of the composite. Particle fracture damage is stochastic in nature and is confined to a small distance from the fracture plane. Minimal void growth is observed, primarily at pre-existing microscopic voids from processing.
3. Microstructure-based simulations, based on 2-D images from the tomography data sets, show the importance of particle distribution and morphology

on the evolution of plastic strain and damage in the composite.

ACKNOWLEDGMENT

Use of the Advanced Photon Source was supported by the United States Department of Energy, Office of Science, Office of Basic Energy Sciences, under Contract No. DE-AC02-06CH11357.

REFERENCES

1. K. Thornton and H.F. Poulsen: *MRS Bull.*, 2008, vol. 33, pp. 587–92.
2. N. Chawla and K.K. Chawla: *Metal Matrix Composites*, Springer, New York, NY, 2006.
3. R.S. Sidhu and N. Chawla: *Mater. Charact.*, 2004, vol. 52, pp. 225–30.
4. M.A. Dudek and N. Chawla: *Mater. Charact.*, 2008, vol. 59, pp. 1364–68.
5. A.J. Kubis, G.J. Shiflet, and R. Hull: *Metall. Mater. Trans. A*, 2004, vol. 35A, pp. 1935–43.
6. D.R.P. Singh, N. Chawla, and Y.-L. Shen: *Mater. Charact.*, 2010, vol. 61, pp. 481–88.
7. F. Lasagni, A. Lasagni, E. Marks, C. Holzzapfel, F. Mucklich, and H.P. Degischer: *Acta Mater.*, 2007, vol. 55, pp. 3875–82.
8. J. Baruchel, P. Bleuet, A. Bravin, P. Coan, E. Lima, A. Madsen, W. Ludwig, P. Pernot, and J. Susini: *C. R. Physique*, 2008, vol. 9, pp. 624–41.
9. J.H. Kinney: *Annu. Rev. Mater. Sci.*, 1992, vol. 22, pp. 121–52.
10. M. Dudek, L. Hunter, S. Kranz, J.J. Williams, S.H. Lau, and N. Chawla: *Mater. Charact.*, 2009, vol. 61, pp. 433–39.
11. N. Chawla, J.J. Williams, X. Deng, and C. McClimon: *Int. J. Powder Metall.*, 2009, vol. 45, pp. 19–27.
12. L. Babout, E. Maire, J.-Y. Buffière, and R. Fougères: *Acta Mater.*, 2001, vol. 49, pp. 2055–66.
13. A. Borbély, F.F. Csikor, S. Zabler, P. Cloetens, and H. Biermann: *Mater. Sci. Eng. A*, 2004, vol. 367, pp. 40–50.
14. P. Kenesei, H. Biermann, and A. Borbély: *Scripta Mater.*, 2005, vol. 53, pp. 787–91.
15. F.A. Silva, J.J. Williams, B.R. Mueller, M.P. Hentschel, P.D. Portella, and N. Chawla: *Metall. Mater. Trans. A*, 2010, vol. 41A, pp. 2121–28.
16. J.J. Williams, Z. Flom, A.A. Amell, N. Chawla, X. Xiao, and F. De Carlo: *Acta Mater.*, 2010, vol. 58, pp. 6194–6205.
17. A. Weck, D.S. Wilkinson, E. Maire, and H. Toda: *Acta Mater.*, 2008, vol. 56, pp. 2919–28.
18. H. Toda, S. Yamamoto, M. Kobayashi, K. Uesugi, and H. Zhang: *Acta Mater.*, 2008, vol. 56, pp. 6027–39.
19. N. Chawla, V.V. Ganesh, and B. Wunsch: *Scripta Mater.*, 2004, vol. 51, pp. 161–65.
20. N. Chawla and K.K. Chawla: *J. Mater. Sci.*, 2006, vol. 41, pp. 913–25.
21. N. Chawla, R.S. Sidhu, and V.V. Ganesh: *Acta Mater.*, 2006, vol. 54, pp. 1541–48.
22. N. Chawla, C. Andres, J.W. Jones, and J.E. Allison: *Metall. Mater. Trans. B*, 1998, vol. 29B, pp. 2843–54.
23. F. De Carlo and B. Tieman: *SPIE*, 2004, vol. 5535, pp. 644–51.
24. F. De Carlo, Y. Chu, D.C. Mancini, and B. Tieman: *SPIE*, 2002, vol. 4503, pp. 1–13.
25. A.G. Peele, F. De Carlo, P.J. McMahon, B.B. Dahl, and K.A. Nugent: *Rev. Sci. Instrum.*, 2005, vol. 76, pp. 083707-1–083707-5.
26. V.V. Ganesh and N. Chawla: *Mater. Sci. Eng.*, 2005, vol. A391, pp. 342–53.
27. N. Chawla, B.V. Patel, M. Koopman, K.K. Chawla, R. Saha, B.R. Patterson, E.R. Fuller, and S.A. Langer: *Mater. Charact.*, 2003, vol. 49, pp. 395–407.